Research Article | Vol. 32, No. 23 / 4 Nov 2024 / Optics Express 41156
Optics EXPRESS

Ultra-efficient surface grating couplers for chip-to-fiber and chip-to-free-space coupling based on single-beam radiation

ALEJANDRO SÁNCHEZ-POSTIGO,[1,*] PABLO GINEL-MORENO,[1,2] JENS H. SCHMID,[3] ABDELFETTAH HADIJ-ELHOUATI,[1,4] ALEJANDRO ORTEGA-MOÑUX,[1] J. GONZALO WANGÜEMERT-PÉREZ,[1] ROBERT HALIR,[1] PAVEL CHEBEN,[3] AND ÍÑIGO MOLINA-FERNÁNDEZ[1]

[1] *Telecommunication Research Institute (TELMA), Universidad de Málaga, E.T.S. Ingeniería de Telecomunicación, Bulevar Louis Pasteur 35, 29010 Málaga, Spain*
[2] *Currently with AGPhotonics S.L., Málaga, Spain*
[3] *Quantum and Nanotechnologies Research Centre, National Research Council Canada 1200 Montreal Rd., Ottawa ON K1A 0R6, Canada*
[4] *Currently with LIGENTEC SA, Lausanne, Switzerland*
[*] *asp@ic.uma.es*

Abstract: Surface grating couplers, such as fiber-chip grating couplers and optical antennas, are fundamental devices in photonic integrated circuits, as they enable the coupling of light between the chip and an external medium. An important metric of surface grating couplers is the coupling efficiency, and high values, greater than -1 dB, are required for applications in quantum technology, light detection and ranging, and optical interconnects. Surface grating couplers typically suffer from radiation loss to the substrate, which significantly limits their coupling efficiency. Here we propose a novel grating-coupling concept that utilizes a high-refractive-index upper cladding to frustrate radiation orders to the substrate by operating in a single-beam diffraction regime. To illustrate this concept, we report the design of an easily fabricable silicon surface grating coupler with an unprecedented coupling efficiency of -0.2 dB to a single-mode optical fiber. Furthermore, the proposed strategy allows us to design an evanescently coupled millimeter-long optical antenna with a coupling efficiency of -0.1 dB to free space. Additionally, an ultra-fast wavelength-tunable beam steering of 0.37°/nm is achieved, which corresponds to more than a 2.5-fold enhancement over comparable silicon antennas. These results represent a pathway for a new set of photonic integrated interfaces for applications in which high-efficiency chip-to-fiber and chip-to-free-space coupling is critical.

1. Introduction

Surface off-chip couplers are standard photonic integrated components for coupling light between high-index-contrast waveguides and the surrounding environment. The most typical of these devices, surface grating couplers, comprise a grating-like perturbed waveguide supporting a leaky mode that is diffracted off-chip. They are typically used as fiber-chip couplers, to efficiently match the mode size of optical fibers and waveguides. Compared to edge couplers, surface grating couplers can be positioned anywhere on the chip, which enables flexible waveguide routing, and exhibit increased robustness to fiber misalignment [1,2]. More recently, surface grating couplers have proven advantageous as optical antennas for free-space coupling and remote-sensing applications such as light detection and ranging (LiDAR). In this scenario, long, weakly emitting surface grating couplers produce sub-0.2° beam divergence, hence high

#537342 https://doi.org/10.1364/OE.537342
Journal © 2024 Received 24 Jul 2024; revised 14 Sep 2024; accepted 23 Sep 2024; published 28 Oct 2024

Optics EXPRESS

angular resolution, and their intrinsic wavelength dependency naturally provides beam-steering capabilities [3].

While high coupling efficiency is always beneficial, some applications are especially sensitive to this performance metric. This is the case for quantum technologies, such as quantum information processing and single-photon LiDAR, as non-classical states of light are rapidly degraded by losses [4]. The fragility of quantum correlations imposes demanding specifications on surface grating couplers, which typically emit an undesired beam to the substrate, where a significant (~40–50%) amount of the input power is dissipated. To mitigate this low directionality, backside mirrors have been utilized to recover downward light, either in the form of metal layers [5–10] or distributed Bragg reflectors [10–13]. However, both types of solutions require complex manufacturing processes [2]. The main alternative consists in breaking the vertical symmetry of the grating teeth to suppress the unwanted beam through destructive interference. By partially etching thicker silicon layers [14–16], using silicon–silicon nitride dual-layer platforms [17], and depositing amorphous or polycrystalline silicon overlays [18], directionalities as high as 80% have been achieved with relatively simple fabrication processes. Blazed surface grating couplers utilize non-rectangular grating elements to reach directionalities exceeding 80% [19–29]. Nevertheless, producing these grating geometries involves several etch steps (e.g., L-shaped and staircase geometries), which introduces demanding mask alignment tolerances [27,29]; multi-level grating structures [22], or slow and difficult focused-ion-beam (FIB) fabrication (e.g., slanted gratings) [30].

In this work, we report a novel surface-grating-coupler concept that yields ~100% directionality without the need for bottom mirrors or non-rectangular grating features. By utilizing a high-refractive-index material (e.g., Si_3N_4), instead of air or SiO_2, as an upper cladding, a phase-matching condition is met for only a single upward beam. Then, a high-refractive-index prism is positioned on top of the cladding to allow the radiated beam to couple off-chip. To illustrate the concept, we present two prism-assisted silicon-on-insulator (SOI) surface grating couplers with a Si_3N_4 cladding operating at a wavelength, λ, of 1.55 μm (see Fig. 1): (a) a fiber-chip coupler with an unparalleled coupling efficiency of -0.2 dB to a single-mode optical fiber and (b) a millimeter-long optical antenna with a coupling efficiency of -0.1 dB to free space. For the latter, an ultra-fast beam-scanning of 0.37°/nm is achieved, which constitutes a 2.5-fold enhancement with respect to comparable optical antennas in the SOI platform. These designs show the potential of this concept for quantum-technology and remote-sensing applications that require ultra-efficient coupling.

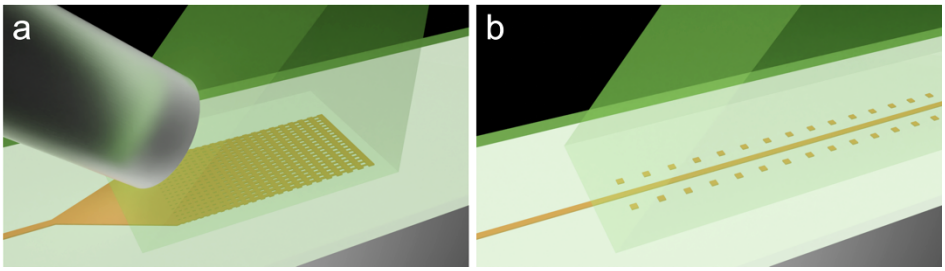

Fig. 1. 3D representations (not to scale) of the devices proposed to illustrate operation in the single-beam radiation regime: (a) a Si_3N_4-cladding, prism-assisted subwavelength-grating-apodized silicon surface grating coupler for fiber-chip coupling, including the optical fiber core, and (b) a Si_3N_4-cladding, prism-assisted, evanescently coupled millimeter-long silicon optical antenna.

The article is organized as follows: In Section 2, the theoretical background of the off-chip single-beam radiation condition is presented, building upon an approach we used to design

Optics EXPRESS

low-loss distributed Bragg deflectors for on-chip shaping of optical beams [31]. Next, Sections 3 and 4 are devoted to the design of exemplary surface grating couplers for chip-to-fiber and chip-to-free-space coupling, respectively. Considerations regarding the material choice of the high-refractive-index prism and its implications for device performance are discussed in Section 5. Finally, conclusions are drawn.

2. Single-beam off-chip radiation condition

Figure 2(a) shows a schematic side view of a standard SOI surface grating coupler formed by a bottom cladding layer (typically SiO_2), a silicon guiding layer, and an upper cladding layer (typically air or SiO_2). Here, the propagation and out-of-chip directions are assumed to be z and y, respectively, while the in-plane direction, x, is considered infinite. The structure comprises a series of silicon segments with a period Λ and a duty cycle $DC = a/\Lambda$. Because of the periodicity, a Floquet–Bloch mode is supported that travels through the grating waveguide with momentum $k_F = k_0 n_F$, where $k_0 = 2\pi/\lambda$ is the wavenumber in vacuum and n_F is the real part of the Floquet–Bloch effective index, i.e., $n_F = \mathrm{Re}\{n_{\mathrm{eff}}\}$. According to the Floquet–Bloch theorem, this mode can be decomposed into a Fourier series, with the mth harmonic having an effective index (real part)

$$n_{F,m} = n_F - m\frac{\lambda}{\Lambda}. \tag{1}$$

This equation shows that the effective indices of consecutive harmonics differ by λ/Λ, as shown in the normalized k-space diagram of Fig. 2(a). The energy of the Floquet–Bloch mode is coupled to a plane wave that freely propagates through the upper or bottom cladding layers when their wave vectors match, i.e.,

$$n_c \sin\theta_c = n_F - m\frac{\lambda}{\Lambda} \tag{2}$$

and

$$n_b \sin\theta_b = n_F - m\frac{\lambda}{\Lambda}, \tag{3}$$

where n_c and n_b are the refractive indices of the upper and bottom cladding layers, respectively, and θ_c and θ_b denote the angular orientation of the corresponding plane waves with respect to the grating vertical. These well-known equations describe the radiation angles of conventional grating couplers [32]. Typically, as illustrated in Fig. 2(a), both expressions are satisfied for $m = 1$, resulting in two diffracted beams, one upward and one downward. In this case, where the upper and bottom cladding layers are assumed infinite, the vertical symmetry of the structure ($n_b = n_c$) ensures a directionality of 50%.

Our proposed design strategy to suppress the downward beam is illustrated in Fig. 2(b). Here, the air ($n_c = n_{air} = 1$) or silicon dioxide ($n_c = n_{SiO_2} = 1.444$) of the top cladding is substituted with a high-refractive-index, transparent material, such that $n_c > n_b$. In this example, we use silicon nitride ($n_c = n_{Si_3N_4} = 2$). This material choice defines a range of possible effective indices of the 1st harmonic for which exclusively Eq. (2) can be fulfilled:

$$-n_c < n_F - \frac{\lambda}{\Lambda} < -n_b. \tag{4}$$

For a given n_F and λ, this single-beam condition can be met by selecting a period Λ that enables upward radiation satisfying

$$-90^\circ < \theta_c < -\arcsin\left(\frac{n_b}{n_c}\right). \tag{5}$$

Thus, not only does the higher refractive index of the top cladding favor upward radiation due to the vertical asymmetry, but the judicious choice of Λ results in a single-beam condition that

Optics EXPRESS

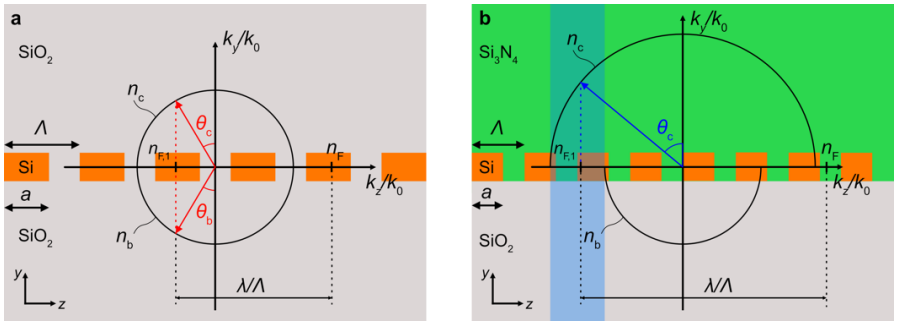

Fig. 2. k-diagram of (a) a standard SiO_2-cladding silicon-on-insulator surface grating coupler that supports both upward and downward diffraction orders, yielding a directionality of 50%, and (b) a Si_3N_4-cladding silicon-on-insulator single-beam surface grating coupler radiating only toward the upper cladding, yielding a directionality of 100%. The highlighted region defines the range of 1st-harmonic effective indices that satisfy the single-beam radiation condition.

forbids a diffracted beam toward the substrate, leading to a theoretical directionality of 100%. This is achieved without the need for blazed (non-rectangular) grating features that suppress downward radiation by destructive interference.

Since surface grating couplers typically radiate into free space ($n_{air} = 1$) or into an optical fiber ($n_{fiber} \sim n_{SiO_2}$) and $n_c > n_{fiber} > n_{air}$, fulfilling the single-beam off-chip radiation condition forces total internal reflection at the upper cladding–air or upper cladding–fiber interfaces. To circumvent this issue, practical devices utilize a prism with a high refractive index $n_p \sim n_c$, as illustrated in Fig. 3.

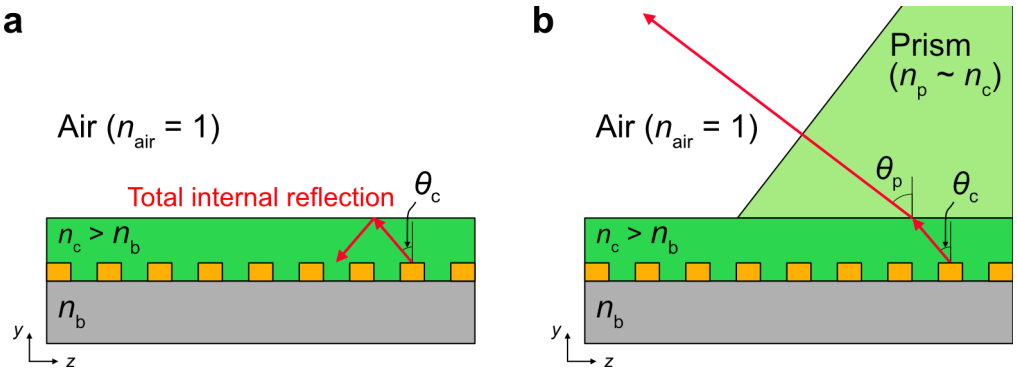

Fig. 3. Schematic representation of a single-beam surface grating coupler (a) with only a high-refractive-index upper cladding, which prevents light from coupling off-chip due to total internal reflection at the cladding-air interface, and (b) with a high-refractive-index prism on top of the high-refractive-index upper cladding, allowing the diffracted beam to couple into free space.

Optics EXPRESS

3. Highly efficient single-beam surface grating coupler for chip-to-fiber coupling

We propose a single-beam surface grating coupler that maximizes the coupling efficiency to a single-mode optical fiber at a wavelength of 1.55 μm for TE polarization. 3D, side-view and top-view schematic representations of the structure are shown in Figs. 1(a), 4(a), and 4b, respectively. The coupler is designed for a 220-nm-thick silicon ($n_{Si} = 3.476$) layer and a 3-μm-thick buried oxide ($n_b = n_{BOX} = 1.444$). A silicon grating encompassing radiative elements with variable pitch $\Lambda_z(z)$ and constant duty cycle DC_z is superimposed on a transverse non-diffractive subwavelength grating (SWG) with constant pitch Λ_x and variable duty cycle $DC_x(z)$. The diffracting grating ensures radiation with a specific angle and the subwavelength grating modulates the radiation strength (SWG apodization). A 2-μm-thick upper cladding layer of Si_3N_4 ($n_c = n_{Si_3N_4} = 2$) is used, on top of which a niobophosphate, high-index prism of Ohara S-NPH3 ($n_p = n_{S-NPH3} = 1.89$ [33]) with an apex angle ψ is positioned. Unlike in other prism-assisted fiber-chip surface grating couplers [34], in this approach the prism is placed flat on the chip surface, without the need for precise alignment at a specific inclination above the chip, as shown in Fig. 4(a). The angles θ_c and θ_p denote the radiation angles in the upper cladding and the prism, respectively. As usual in SOI grating couplers, the grating width is chosen as 15 μm and an adiabatic, 300-μm-long linear taper is used to expand the fundamental mode of a 500-nm-wide input waveguide [35].

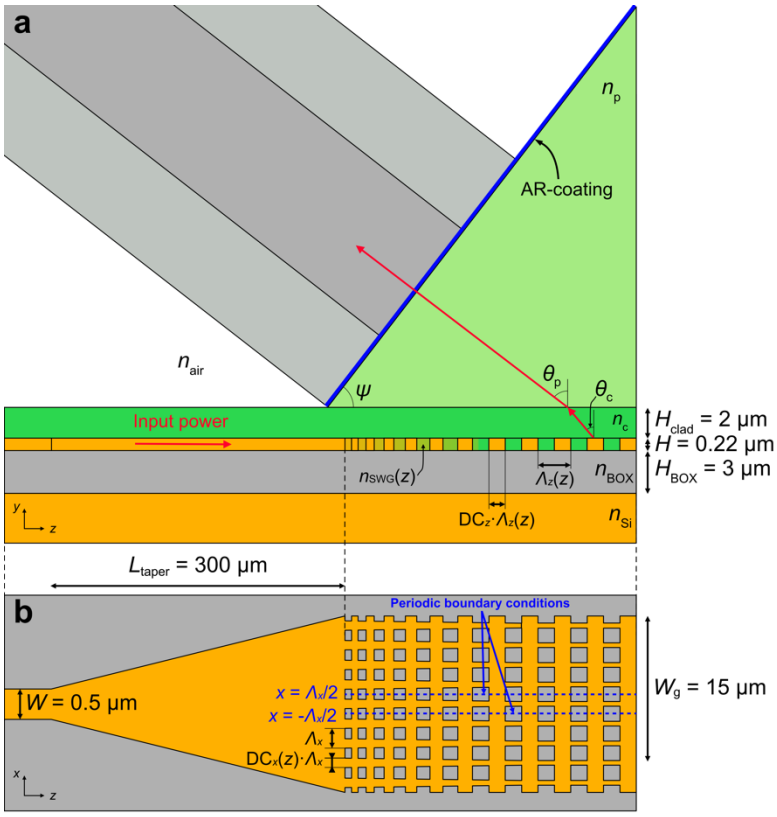

Fig. 4. Schematic representation of the proposed highly efficient SWG-apodized silicon surface grating coupler: (a) side view, (b) top view. The high-refractive-index upper cladding and prism allow for single-beam radiation into a single-mode optical fiber. The figures are not to scale.

Optics EXPRESS

The coupling efficiency (CE) is a key metric of fiber-chip surface grating couplers, defined as the fraction of input guided power that is coupled into the optical fiber. Assuming that no power remains guided at the end of the grating waveguide, the coupling efficiency can be calculated as the product of three factors: the amount of incident power that is not back-reflected into the input waveguide ($1 - R$), the directionality or fraction of power that is radiated upward (D), and the overlap integral (OL) between the radiated field and the mode field of the optical fiber, i.e., CE = $(1 - R) \cdot D \cdot$ OL [36]. To optimize CE, all three parameters need to be maximized simultaneously, which is challenging because they depend on the geometrical parameters of the grating features. For example, grating apodization typically requires careful selection of the length, duty cycle, and etch steps of each grating tooth to radiate a Gaussian-like field profile at a given angle while also ensuring high directionality. On the contrary, our proposed strategy allows us to decouple the maximization of the directionality from that of the other factors, thereby substantially simplifying the design procedure. In this scheme, $D \sim 1$ regardless of the geometry of the grating features provided that the single-beam condition [Eq. (4)] is met. Then, optimum values for R (~ 0) and OL (~ 1) can be attained by apodizing, i.e., varying the radiation strength, α_F, along the propagation direction to synthesize a specific field profile.

Rather than controlling α_F by smoothly adjusting the duty cycle DC_z, which leads to impractically small feature sizes, in this work we leverage SWG metamaterial apodization [35]. Since its conception for silicon photonics, SWG metamaterial engineering has fueled the development of groundbreaking integrated devices [36–38]. As shown in Fig. 4, the transverse SWG pattern behaves as a homogeneous metamaterial with an equivalent refractive index, n_{SWG}, between n_{Si} and $n_{Si_3N_4}$. In our device, the range of possible n_{SWG} values depends on the period Λ_x and duty cycle DC_x of the grating.

First, using our in-house eigenmode expansion (EME) simulator [39], we analyze the fundamental Floquet–Bloch mode guided by a periodic grating of pitch Λ_z. The duty cycle DC_z is fixed at 50% to maximize the minimum feature size (MFS) in the propagation direction. For a SiO_2 bottom cladding and a Si_3N_4 upper cladding, Eq. (5) shows that the grating must radiate backward at $|\theta_c| > 46.2°$ to guarantee single-beam operation. Figure 5(a) shows the radiation angle, obtained from n_F through Eq. (2), as a function of the longitudinal period Λ_z and n_{SWG}. For a transverse period Λ_x of 450 nm, the values of n_{SWG} synthesizable for MFS > 90 nm range from 2.2 to 3.1 [37]. In the figure, only radiation angles that meet the single-beam condition are shown. The red line indicates the pair (Λ_z, n_{SWG}) for which θ_c = -55°. This angle is sufficiently far away from the lower bound of the single-beam window, while leading to relatively low wavelength dispersion, as discussed in Section 5. For the chosen (Λ_z, n_{SWG}) values, Fig. 5(b) shows the radiation strength, calculated from the imaginary part of the Floquet–Bloch effective index ($\alpha_F = k_0 \mathrm{Im}\{n_{eff}\}$).

Under the assumption that the previous Floquet–Bloch analysis holds for slowly varying grating teeth, the next step is to map the $\alpha_F(\Lambda_z)$ and $\alpha_F(n_{SWG})$ profiles of Fig. 5(b) to the target $\alpha_F(z)$ profile in Fig. 5(c) (red line). The chosen $\alpha_F(z)$ synthesizes a near Gaussian field amplitude (blue line) conveying ~100% of the input power and theoretically leading to a ~96% overlap with a single-mode optical fiber with a mode field diameter of 10.4 μm at 55° tilt. The synthesized field profile is computed as the square root of the radiated power per unit length, $P_{rad}(z) = 2\alpha_F(z)P(z)$ [32], where $P(z) = P_0 \exp(-2\int_0^z \alpha_F(t)\mathrm{d}t)$ is the remaining power at position z in the grating, and P_0 is the input power. The abrupt start in the field profile is caused by the minimum achievable α_F of ~0.01 μm^{-1}. This mapping procedure results in apodization functions $\Lambda_z(z)$ and $n_{SWG}(z)$, shown in Fig. 5(d). Finally, for the practical implementation of the structure, by using the technique described in [37], the equivalent metamaterials with refractive index $n_{SWG}(z)$ are translated into actual transverse SWG structures with a constant pitch Λ_x of 450 nm and a duty cycle $DC_x(z)$. By following this apodization methodology, all features are larger than 90 nm, which is within the range of most typical e-beam and deep-UV lithography tools.

Optics EXPRESS

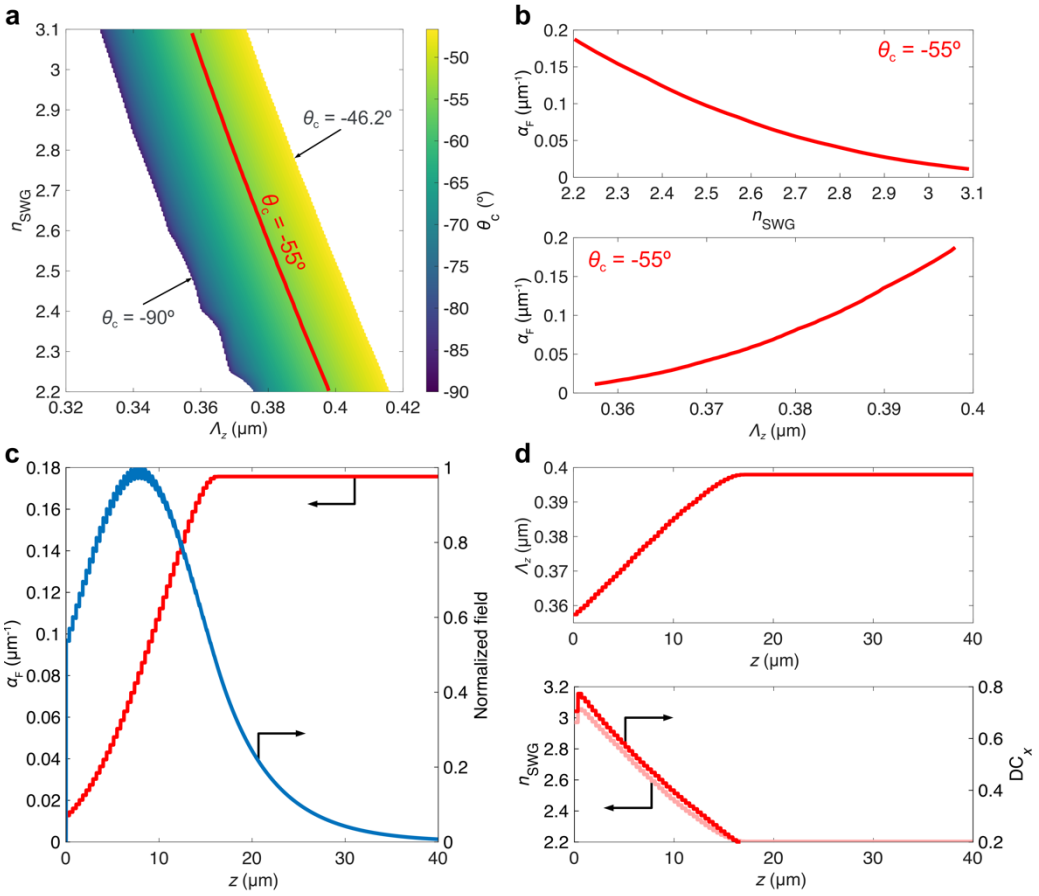

Fig. 5. Design procedure based on Floquet–Bloch analysis of a single transverse SWG homogenized period. (a) Radiation angle θ_c of a single-beam SWG-metamaterial surface grating coupler as a function of the period length Λ_z and the equivalent refractive index n_{SWG}. The red line highlights $\theta_c = -55°$, which guarantees that a single beam will be radiated by the structure. (b) Coupling strength (α_F) for the values of Λ_z and n_{SWG} that ensure $\theta_c = -55°$ obtained from (a). (c) Target α_F profile (red) and its synthesized field (blue). (d) Apodization functions [$\Lambda_z(z)$, $n_{SWG}(z)$, and $DC_x(z)$] obtained by mapping the $\alpha_F(n_{SWG})$ and $\alpha_F(\Lambda_z)$ functions in (b) to the target $\alpha_F(z)$ profile in (c).

We simulate the full structure using RSoft FullWAVE 3D finite-diference time-domain (3D-FDTD) software [40]. As in [35], in order to avoid computational burden, a single transverse SWG period is included in the simulation window, imposing periodic boundary conditions at $x = -\Lambda_x/2$ and $x = \Lambda_x/2$ to emulate an infinitely wide grating (see Fig. 4(b)). A fundamental TE slab mode is used to excite the Floquet–Bloch mode of the grating waveguide. To minimize the beam divergence, a custom single-mode optical fiber with a cladding diameter of 30 μm, which can be placed close to the chip surface, is employed. In the simulations, the optical fiber is in physical contact with the Ohara S-NPH3 prism, while an index-matching gel could be used for practical realizations. Fresnel reflection loss is minimized by a single-layer quarter-lambda anti-reflection (AR) coating [refractive index $n_{\lambda/4} = (n_{S-NPH3} \cdot n_{fiber})^{1/2} = 1.66$, thickness $l_{\lambda/4} = 0.25\lambda/n_{\lambda/4} = 0.23$ μm] on the prism surface. Since the design procedure is based on a 2D Floquet–Bloch analysis that does not account for the refractive index of Ohara S-NPH3, a

Optics EXPRESS

simple refinement of the prism and fiber angles is performed. Figure 6 provides the 3D-FDTD propagation of the electric field traveling through the grating and coupled into the optical fiber, tilted at an angle $\phi_{\text{fiber}} = \psi = 57.8°$ above the surface grating coupler. From the figure, it is apparent that virtually all power is radiated upward. Specifically, a monitor above the grating collects ~99% of the input power. The remaining ~1% is attributable to back-reflections into the input port and reflections at the upper cladding–prism interface, as well as minor scattering in the waveguide-grating transition. An unprecedented peak coupling efficiency of 95.5% (-0.20 dB) is achieved at a center wavelength of 1.55 μm, with a 1-dB bandwidth of 15 nm (see Fig. 7(a)). These results demonstrate the effectiveness of a single-beam design to increase the overall efficiency of fiber-chip surface grating couplers, potentially reaching 100%.

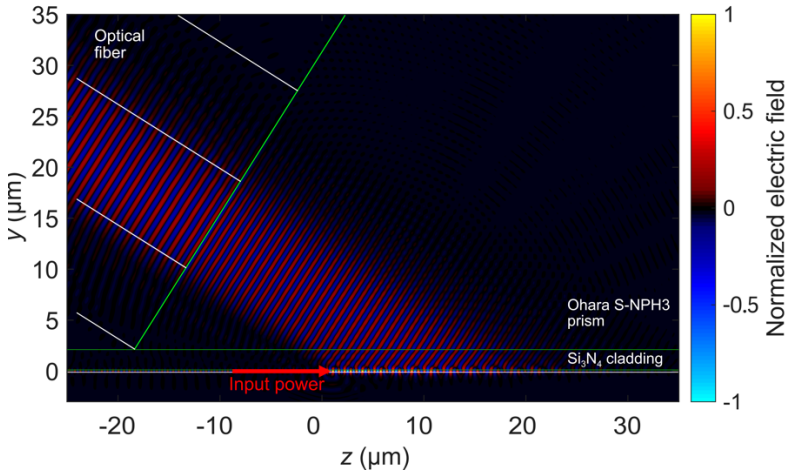

Fig. 6. 3D-FDTD simulation of the real part of the electric field propagation through the designed single-beam surface grating coupler at a wavelength of 1.55 μm. The TE-polarized radiated field is coupled into a custom optical fiber with a cladding diameter of 30 μm to facilitate positioning above the chip.

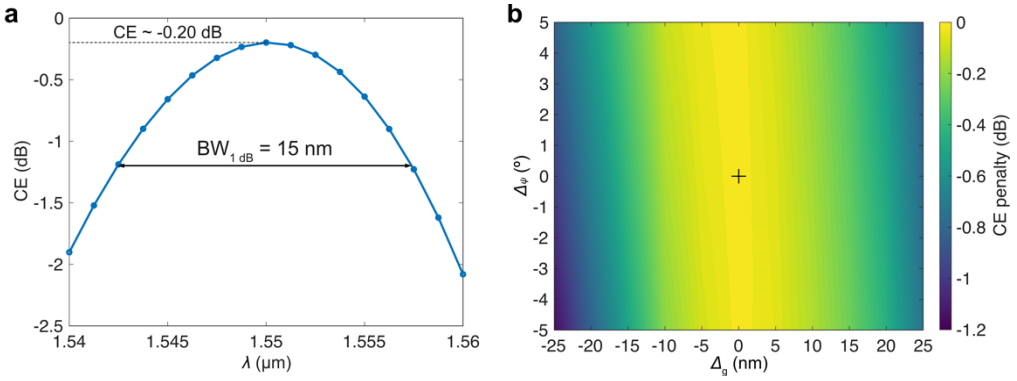

Fig. 7. (a) Calculated coupling efficiency of the designed single-beam fiber-chip surface grating coupler as a function of the wavelength for TE polarization. (b) Tolerance analysis: estimated coupling-efficiency penalty versus fabrication errors in the grating features (Δ_g) and variations in the prism apex angle (Δ_ψ) at a wavelength of 1.55 μm. The cross marks the nominal design ($\Delta_g = \Delta_\psi = 0$).

Optics EXPRESS

We also study the influence of deviations from the nominal design on the coupling efficiency at a wavelength of 1.55 μm. For this analysis, we assume that an index-matching gel is used and that the optical fiber can be reoriented to optimize the coupled power, as in conventional surface grating couplers. Figure 7(b) shows the estimated coupling-efficiency degradation for variations Δ_ψ in the prism angle ($\psi + \Delta_\psi$) and for fabrication errors Δ_g in the grating features ($DC_z + \Delta_g/\Lambda_z$, $DC_x + \Delta_g/\Lambda_x$). Since ψ is selected for normal incidence (i.e., minor refraction at the prism output surface), the penalty in the coupling efficiency due to Δ_ψ is minimal. For prism deviations $\Delta_\psi = \pm 1°$, fabrication errors $\Delta_g = \pm 25$ nm result in a maximum CE penalty of -1 dB, while a degradation of only -1.15 dB is predicted for an unrealistically large prism error $\Delta_\psi = -5°$. This tolerance to fabrication imperfections is comparable to that of other high-efficiency surface grating couplers [27]. Additionally, we examined the effect of variations in the thickness of the silicon layer, estimating a negligible penalty within a typical range of ±10 nm.

Finally, since single-mode optical fibers with a cladding diameter of 30 μm are not commercially available, we suggest the following alternatives for implementing the proposed fiber-chip surface grating coupler: (i) polishing and shaping the tip of a standard 125-μm-cladding optical fiber to facilitate positioning; (ii) using an off-the-shelf, 80-μm-cladding RC-SMF optical fiber [41], for which we estimate a 0.54-dB CE penalty due to beam divergence, and (iii) designing a self-imaging grating structure that focuses the radiated beam on the input aperture of a standard optical fiber, thereby compensating for beam-divergence expansion [21].

4. Highly efficient single-beam surface grating antenna for chip-to-free-space coupling

In [42,43], we presented a novel type of optical antenna for use in one-dimensional optical phased array (1D-OPA) configurations for LiDAR and other beamforming and scanning applications. The antenna consists of a long SOI waveguide that is evanescently coupled to lateral silicon blocks separated from the core. These loading blocks are arranged with a periodicity that satisfies the grating-coupler equation [Eq. (2) and Eq. (3)], thereby enabling off-chip diffraction. An important advantage of this approach is that weak grating coupling strength can be achieved with MFS > 80 nm, rather than 8–10 nm of typical waveguide-corrugated grating antennas [44], therefore facilitating the fabrication of millimeter-long antennas via deep-UV lithography. Due to the large scale of the antenna, a highly collimated far-field is obtained. Specifically, we reported a minimum divergence of 0.025° (theoretical)/0.1° (experimental). Beam-steering in the elevation direction (yz plane) is attained by tuning the wavelength of the laser, which changes the radiation angle as Eq. (2) dictates, and a wavelength sensitivity of ~0.14°/nm (theoretical)/~0.13°/nm (experimental) is achieved. However, according to our simulations, the coupling efficiency to free space, calculated as $CE = (1 - R) \cdot D \sim D$ (assuming all power is radiated), is only -2.4 dB. Here, this antenna is improved by operating in the single-beam regime, thereby maximizing the directionality up to ~99% (virtually 0 dB). The high directionality also eliminates reflections at the bottom cladding–substrate interface, which can lead to undesired destructive interference at specific emission angles [25]. Furthermore, as a beneficial byproduct of our proposed single-beam design approach, the scanning velocity is enhanced by a factor of ~2.5, resulting in 0.37°/nm. Moreover, the absence of an optical fiber for chip-to-free-space applications substantially simplifies packaging compared to the fiber-chip surface grating coupler discussed in Section 3.

An artistic representation of a single antenna is shown in Fig. 1(b), while technical top and side views are schematized in Fig. 8. The antenna is designed for a 220-nm-thick SOI substrate with a buried oxide of 3 μm. The millimeter-long waveguide core (width W) is loaded with an arrangement of lateral radiative blocks (width W_s, period Λ, duty cycle $DC = L_s/\Lambda$), which are separated by a distance g from the waveguide core. A 2-μm-thick Si_3N_4 cladding is deposited, on top of which an AR-coated Ohara S-NPH3 prism (apex angle ψ) is placed. The

Optics EXPRESS

AR coating comprises a single layer with refractive index $n_{\lambda/4} = (n_{\text{S–NPH3}} \cdot n_{\text{air}})^{1/2} = 1.37$ and thickness $l_{\lambda/4} = 0.25\lambda/n_{\lambda/4} = 0.28$ μm. The coupler is designed to operate at a central wavelength of 1.55 μm for TM polarization, which is preferred for long optical antennas [42].

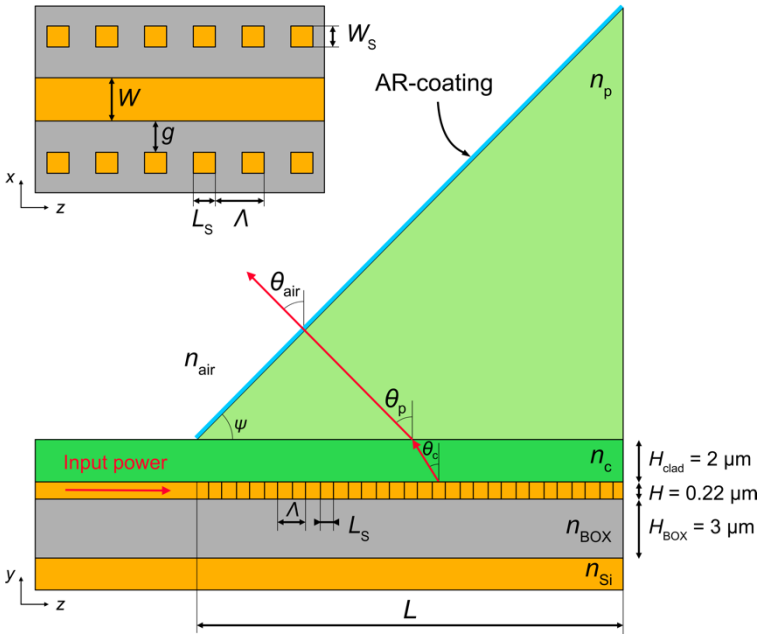

Fig. 8. Schematic top-view and side-view representations of the proposed evanescently coupled millimeter-long optical antenna.

Since the lateral grating introduces only a weak perturbation into the waveguide core, the single-beam condition allows us to decouple the optimization of the coupling efficiency from that of other metrics, such as the beamwidth. Our design methodology is summarized as follows: First, a non-loaded waveguide width (W) is chosen that ensures single-mode operation, minimizes leakage losses to the silicon substrate, and delocalizes the supported mode. The latter decreases scattering caused by sidewall roughness and allows for an increased gap between the waveguide core and the lateral gratings, thus simplifying fabrication. Second, it is assumed that the real parts of the effective indices of the non-loaded and loaded waveguides are virtually identical due to the weak perturbation. Thus, the period Λ can be estimated from Eq. (2) by using the effective index of the non-loaded waveguide, to enable radiation at an angle θ_c that meets the single-beam condition at the central operating wavelength [Eq. (5)]. Third, using RSoft FullWAVE, a rigorous 3D Floquet–Bloch analysis of an antenna period is carried out [45], from which α_F is obtained as a function of the geometry and position of the lateral grating (L_s, W_s, g). These parameters allow for precise control of α_F, while maintaining the coupling efficiency nearly unaffected due to operation in the single-beam regime. For a target α_F, the antenna length, L, is selected to radiate 99% of the input power into the upper cladding. Finally, the performance of the designed antenna is evaluated by analyzing the far-field of the emitted beam. This is efficiently computed by concatenating the Floquet–Bloch mode fields of all antenna periods, thereby constructing the near-field, and then obtaining its two-dimensional Fourier transform (Fraunhofer diffraction integral). A detailed description of this procedure can be found in [42].

Optics EXPRESS

For a given 3-dB far-field beamwidth, $\delta\theta_{air}$, the required grating strength, α_F, can be estimated from [42]

$$\delta\theta_{air} \approx \frac{2\alpha_F}{k_0 \cos(\theta_{air})}, \tag{6}$$

where θ_{air} is the expected radiation angle of the far-field emitted beam in the air. In our design, we aim for $\delta\theta_{air} \sim 0.04°$. Assuming a radiation angle θ_{air} between -50° and -70°, α_F in the range 0.5–0.9 mm^{-1} is required. For a core width (W) of 500 nm, the real part of the effective index of the fundamental mode is 2.146. For this value, $\Lambda = 410$ nm enables upward radiation with $\theta_c \sim$ -54.8° ($\theta_p \sim$ -59.8°), which is within the single-beam range. To achieve normal incidence at the nominal wavelength of 1.55 µm, a prism with $\psi = 59.8°$ is therefore selected (see Fig. 9(b), inset). The segment length (L_s) is chosen as 120 nm for simplicity. The simulated radiation strength is shown as a function of the gap length (g) and the segment width (W_s) in Fig. 9(a). For $g = 240$ nm, which ensures a weak perturbation, $W_s = 120$ nm is chosen, yielding $\alpha_F \sim 0.54$ mm^{-1} at the nominal wavelength of 1.55 µm. This α_F value leads to $L \sim 4.25$ mm.

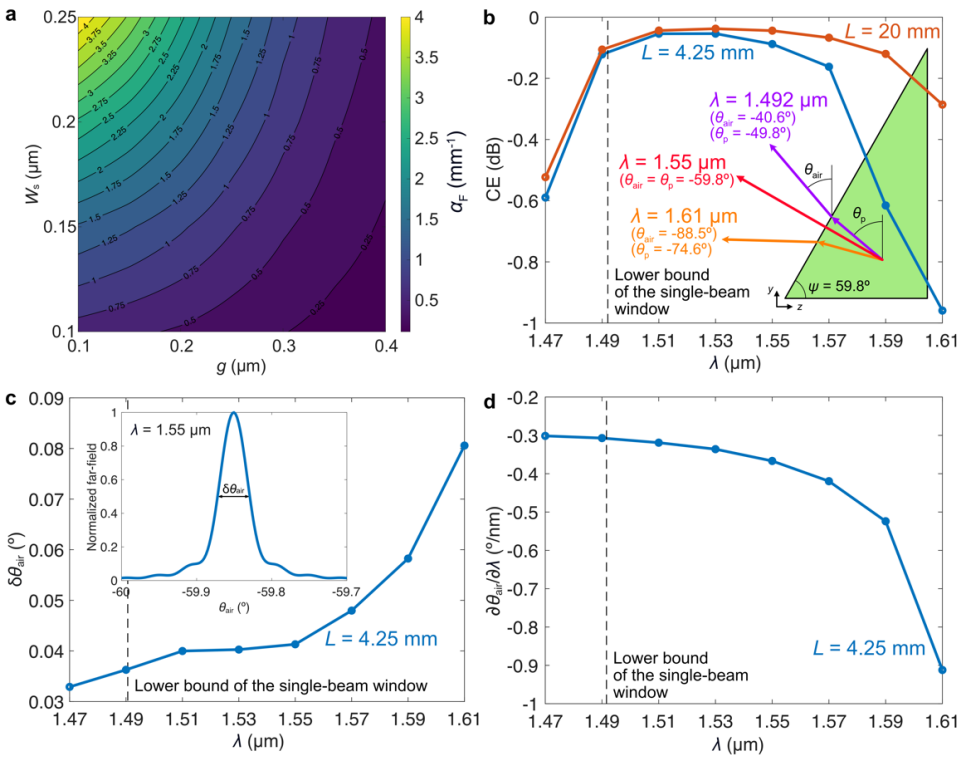

Fig. 9. (a) Grating strength (α_F) as a function of the width of the radiative lateral segments (W_s) and the gap between them and the waveguide core of the antenna (g), assuming a segment length (L_s) of 120 nm and a core width (W) of 500 nm, for TM polarization at the nominal wavelength ($\lambda = 1.55$ µm). (b) Coupling efficiency to free space as a function of the wavelength for the designed antenna, with a length $L = 4.25$ mm (blue curve), and for an antenna with $L = 20$ mm (orange curve). Inset: radiation angles in the prism and in free space for $\lambda = 1.55$ µm (nominal), $\lambda = 1.49$ µm, and $\lambda = 1.61$ µm. (c) Beamwidth in the elevation direction (yz plane) as a function of the wavelength for the designed antenna ($L = 4.25$ mm). Inset: radiation pattern as a function of the radiation angle in free space at the nominal wavelength ($\lambda = 1.55$ µm). (d) Scanning sensitivity in free space as function of the wavelength for the designed antenna ($L = 4.25$ mm).

Optics EXPRESS

From a horizontal power monitor in the Si_3N_4 layer, we calculate the coupling efficiency into the upper cladding. Then, we add the transmission penalty that is due to minimal reflections at the upper cladding–prism and prism-air interfaces. A coupling efficiency into free space of ~98% (-0.09 dB) is obtained at 1.55-μm wavelength, with values higher than ~80% (-0.96 dB) in the wavelength range (see Fig. 9(b), blue curve). As schematized in the inset, the represented wavelength range corresponds to the field-of-view from the lower bound of the single-beam window ($\theta_{air} \sim$ -41°, $\lambda \sim$ 1.49 μm) to almost horizontal radiation into free space ($\theta_{air} \sim$ -89°, $\lambda \sim$ 1.61 μm). The excellent directionality is due to operation in the single-beam regime. At wavelengths below ~1.49 μm, the single-beam condition is no longer satisfied, resulting in an CE drop. At longer wavelengths, the reduced CE is caused by a smaller α_F compared to the design value at 1.55 μm, and higher CE could be achieved by increasing the antenna length, as shown in Fig. 9(b), orange curve.

The far-field pattern of the antenna is computed from a near-field cut obtained from a horizontal field monitor in the upper cladding. The normalized field at $\lambda = 1.55$ μm is shown as a function of the radiation angle in the air, θ_{air}, in Fig. 9(c) (inset). The full width at half maximum (FWHM) of this pattern indicates a beamwidth $\delta\theta_{air}$ of 0.041°. Figure 9(c) also provides the far-field beamwidth as a function of the wavelength, being less than 0.09° in the entire simulated band from 1.47 μm to 1.61 μm. Furthermore, a scanning sensitivity in the air of 0.37°/nm is predicted around the design central wavelength (see Fig. 9(d)), which is more than 2.5-fold improvement with respect to the steering rate of similar antennas in SOI [43]. A discussion about the rationale for this significant enhancement is given in Section 5.

5. Discussion

In the simulations of Sections 3 and 4, we chose an Si_3N_4 cover as an upper cladding because layers of this material can be deposited by plasma-enhanced chemical vapor deposition (PECVD). To avoid total internal reflection, we additionally used a discrete prism made of Ohara S-NPH3, a relatively inexpensive and machinable optical glass proprietary to Ohara Inc., with a refractive index close to that of Si_3N_4 and low chromatic dispersion ($\partial n_{S-NPH3}/\partial\lambda$ = -0.027 μm^{-1} at 1.55-μm wavelength) [33,46]. However, other options are available. For example, SU-8 is a common epoxy-based photoresist that can be easily spin-coated and offers a refractive index of 1.59 in the telecom band. A similar refractive index is offered by Nanoscribe IP-n162 photoresin, intended for direct-laser-writing of freeform optical structures, including microprisms, by two-photon polymerization [47].

An obvious choice of upper-cladding and prism materials is determined by the integrated platform, since index contrast is required for vertical mode confinement. For example, both Si_3N_4 and SU-8 are valid materials for SOI, but only the latter could be employed in Si_3N_4-on-insulator platforms. Recent SU-8 waveguides [48], on the other hand, need even lower-refractive-index materials, which dramatically reduce the size of the single-beam window.

Indeed, depending on the application, the range of effective indices that satisfy the condition may significantly impact the performance of the single-beam coupling devices. In the following, we examine the relationship between the prism refractive index and the performance metrics of SOI single-beam off-chip couplers. Subsequently, we provide a set of guidelines to help with the selection of the appropriate materials. For this study, without loss of generality, we assume that the grating radiates directly into the prism, as the momentum conservation [Eq. (2)] holds for the prism just as it does for the upper cladding. For simplicity, we consider coupling from the prism into free space, although the same analysis applies when coupling into an optical fiber or an index-matching gel.

A useful parameter in surface grating couplers is the range of feasible radiation angles that can be scanned in the air by tuning the laser wavelength ($\Delta\theta_{air}$). This corresponds to the angular bandwidth of fiber-chip couplers or the field-of-view in the elevation direction of 1D-OPA

Optics EXPRESS

antennas. In the context of this article, as illustrated in Fig. 10(a), the field-of-view $\Delta\theta_{air}$ is determined by the radiation angles in the range (θ_{air} = -90°, $\theta_{air} = 90° - \psi$) that satisfy the off-chip single-beam condition. Figure 10(b) shows the radiation angle in the air, θ_{air}, as a function of the radiation angle in the prism, θ_p, by application of the Snell's law, for Ohara S-NPH3 and Nanoscribe IP-n162 prisms with different angles ψ, for SOI substrates. The higher the refractive index of the prism, the higher the width of the single-beam window, hence the larger $\Delta\theta_{air}$. Likewise, because of the refraction at the prism-air interface, using prisms with higher ψ also expands $\Delta\theta_{air}$.

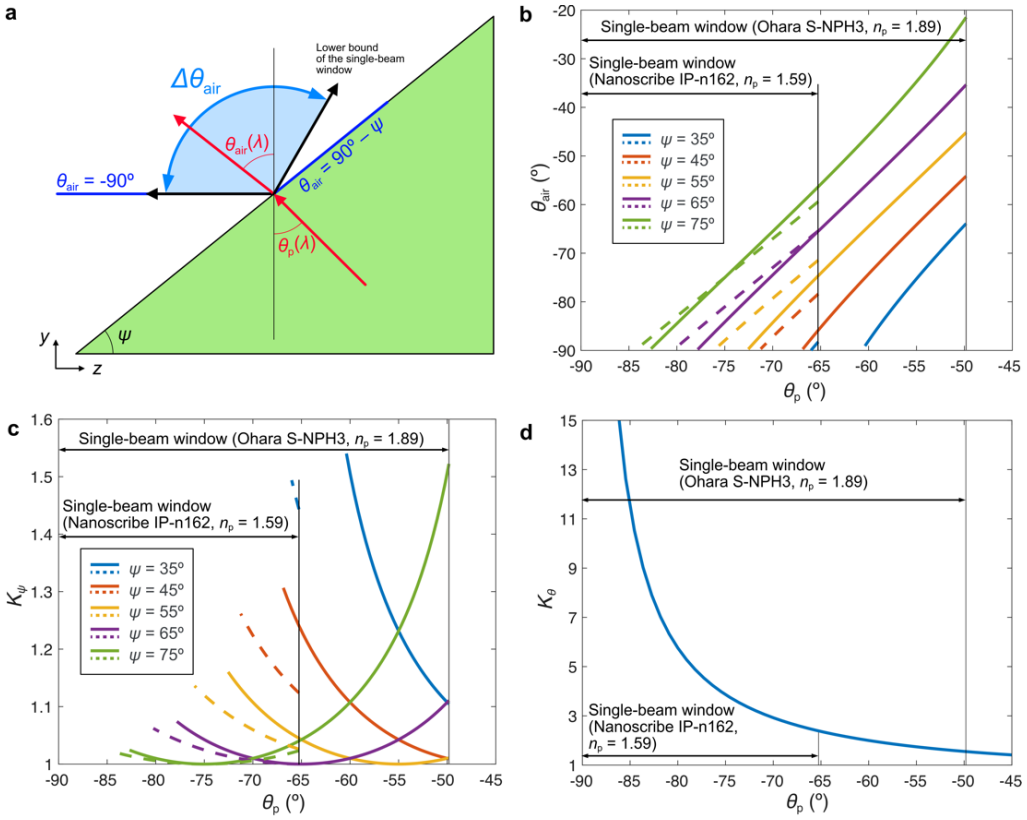

Fig. 10. (a) Diagram of the refraction of a radiated beam at the prism-air interface. (b) Radiation angle in the air as a function of the radiation angle in the prism for several Ohara S-NPH3 (solid lines) and Nanoscribe IP-n162 (dashed lines) prisms with different apex angles. The ranges of angles in the air define the achievable field-of-view $\Delta\theta_{air}$, which is graphically defined in (a). (c) Obliquity factor K_ψ as a function of the radiation angle in the prism, for the same prisms as in (b). (d) Obliquity factor K_θ.

The range $\Delta\theta_{air}$ is related to the wavelength sensitivity, $\partial\theta_{air}/\partial\lambda$, an important figure of merit in surface grating couplers. Specifically, the bandwidth of fiber-chip couplers, usually defined as the range of wavelengths for which the peak coupling efficiency drops by 1 dB, is inversely proportional to this metric. For 1D-OPA optical antennas, the wavelength sensitivity denotes the scanning velocity in the elevation plane. By taking derivative from Eq. (2), the wavelength sensitivity of the beam radiated into the prism of a single-beam off-chip coupler becomes

$$\frac{\partial\theta_p}{\partial\lambda} = \left[\frac{\partial n_F}{\partial\lambda} - \frac{1}{\Lambda} - \frac{\partial n_p}{\partial\lambda}\sin(\theta_p)\right]\frac{1}{n_p\cos(\theta_p)} \approx \left(\frac{\partial n_F}{\partial\lambda} - \frac{1}{\Lambda}\right)\frac{1}{n_p\cos(\theta_p)}, \tag{7}$$

Optics EXPRESS

where the approximation arises from considering $\partial n_p/\partial\lambda$ negligible. The radiated beam is refracted at the prism-air interface, resulting in a wavelength sensitivity in the air

$$\frac{\partial\theta_{air}}{\partial\lambda} = \frac{\sin(\theta_p+\psi)}{n_{air}\cos(\theta_{air}+\psi)}\frac{\partial n_p}{\partial\lambda} + \frac{n_p\cos(\theta_p+\psi)}{n_{air}\cos(\theta_{air}+\psi)}\frac{\partial\theta_p}{\partial\lambda} \approx \frac{1}{n_{air}}\underbrace{\left(\frac{\partial n_F}{\partial\lambda}-\frac{1}{\Lambda}\right)}_{K_i}\underbrace{\frac{\cos(\theta_p+\psi)}{\cos(\theta_{air}+\psi)}}_{K_\psi\,\geq\,1}\underbrace{\frac{1}{\cos(\theta_p)}}_{K_\theta\,\geq\,1}, \tag{8}$$

where K_i denotes the intrinsic wavelength dispersion of the grating, and K_θ and K_ψ are obliquity factors. In this discussion, we will focus on K_θ and K_ψ, because K_i, although affected by the upper medium through n_F, depends on many geometrical parameters that are not directly related to the single-beam concept, such as the width of the waveguide core or the grating period.

Factor K_ψ accounts for the light refraction at the prism-air interface. In Fig. 10(c), K_ψ is plotted against the radiation angle θ_p for the prisms and θ_p values that produce valid θ_{air} angles in Fig. 10(b). When the radiated beam impinges perpendicularly into the interface ($\theta_p = -\psi$), $K_\psi \sim 1$. Steeper oblique incidence can be produced by significantly detuning the radiation angle and the prism angle, thereby increasing K_ψ. For Ohara S-NPH3 prisms, $K_\psi \sim 1.5$ can be achieved for $(\theta_p, \psi) \sim (-50°, 75°)$ and $(-60°, 35°)$. Similarly, for Nanoscribe IP-n162 prisms, $K_\psi \sim 1.5$ for $(\theta_p, \psi) \sim (-65°, 35°)$. Even though these operation points provide about 50% amplification in the wavelength sensitivity with respect to the intrinsic value (K_i), they lead to radiated beams in the air that are very close to the limits of the $\Delta\theta_{air}$ range. Besides, because of the refraction law, the diameter of the radiated field transmitted into the air is also reduced by K_ψ, which increases the beam divergence. For these reasons, typical devices are designed for $K_\psi \sim 1$.

The most relevant term is the obliquity factor K_θ, which is common to all types of surface grating couplers. It designates the increase in the wavelength sensitivity due to angular deviations with respect to the normal orientation. Figure 10(d) shows K_θ as a function of the radiation angle in the prism. For perfectly vertical radiation into the prism ($\theta_p = 0$), there is no amplification of the intrinsic wavelength sensitivity ($K_\theta = 1$). On the contrary, when $\theta_p = -90°$, K_θ tends asymptotically to infinity, producing maximum dispersion. It is clear from the figure that the single-beam condition limits the range of possible radiation angles to those in the leftmost region of the curve, where amplification is highest. Consequently, single-beam surface grating couplers naturally exhibit a high wavelength sensitivity. The lower the refractive index of the prism, the narrower the single-beam window, hence higher sensitivity, yet at the expense of reduced field-of-view (small $\Delta\theta_{air}$).

These considerations show that, for typical use cases, such as those presented in this article, single-beam surface grating couplers benefit from using prism materials with the highest possible refractive indices that fulfill the single-beam condition:

- *For fiber-chip couplers*, extending the single-beam window allows designers to choose a radiation angle that is closer to the vertical, thereby increasing the bandwidth. For a refractive index $n_p = 1.89$, the lower bound of the single-beam condition is $\theta_p = -49.8°$. However, if a prism of Nanoscribe IP-n162 is used, the lower radiation angle of the single-beam regime is -65.3°, yielding a bandwidth reduction of $\cos(-65.3°)/\cos(-49.8°) \sim 0.65$. In contrast, the bandwidth could be broadened by utilizing upper cladding and prism materials with higher refractive indices, such as chalcogenide glasses ($n_p \sim n_c \sim 2.5$) [49], or by undercutting the SiO_2 bottom cladding ($n_b = 1$). However, these methods may require more complex manufacturing and handling processes compared to using SiO_2, Si_3N_4, and Ohara S-NPH3 for the bottom cladding, upper cladding, and prism materials, respectively. This rationale justifies our choice of materials for the chip-to-fiber coupler described in Section 3. We selected a radiation angle $\theta_p \sim -60°$ to operate near the lower bound of the single-beam window, thus closer to the grating normal. The achieved 1-dB bandwidth of 15 nm is narrower than that of conventional high-efficiency fiber-chip surface grating couplers [11,14], which radiate at around ±10°, by a factor of $\cos(-60°)/\cos(\pm10°) \sim 0.5$.

Optics EXPRESS

- *For 1D-OPA optical antennas*, a large single-beam regime provides increased field-of-view, which is essential for beam-steering applications, as well as design flexibility. Lower-refractive-index prisms impose high wavelength sensitivity, but also large beam divergence, low field-of-view, and the use of prisms with fragile sharp angles. Interestingly, when using higher-refractive-index prisms, identical wavelength sensitivity and beam divergence can be obtained by increasing the radiation angle, while maintaining a large field-of-view. Thus, depending on the specifications of their application, by using high-refractive-index prisms designers can privilege (a) high wavelength sensitivity, by working at higher radiation angle, or (b) narrow beamwidth, by operating at lower radiation angles.

6. Conclusion

In this work, we have presented a novel and simple design strategy for off-chip surface grating couplers with ∼100% directionality. The concept exploits the relationship between the refractive indices of the waveguide materials to enable only a single beam radiated upward, avoiding diffraction toward the substrate, thus maximizing the directionality. Multiple waveguide platforms can benefit from this single-beam diffraction condition, provided that the refractive index of the upper medium is higher than that of the bottom cladding. Specifically, an SOI waveguide with a Si_3N_4 top cladding is utilized to design an SWG-apodized surface grating coupler with unparalleled 95.5% (-0.2 dB) coupling efficiency to a single-mode optical fiber at a wavelength of 1.55 µm. Furthermore, an Si_3N_4-cladding SOI optical antenna is proposed, achieving a coupling efficiency of -0.1 dB to free space and a scanning rate of 0.37°/nm at a wavelength of 1.55 µm. We believe this work holds promise for the development of off-chip surface couplers specifically focused on ultra-efficient performance, such as grating couplers for quantum technologies, fast-steering optical antennas for sensing and object-tracking applications, and low-loss optical interconnects in data centers.

Funding. National Research Council Canada (HTSN 209, STR2-0102); Ministerio de Ciencia, Innovación y Universidades (PDC2023-145833-I00, TED2021-130400B-I00/ AEI/10.13039/501100011033/ Unión Europea NextGeneration EU/PRTR, PID2023-151178OB-I00); Universidad de Málaga.

Disclosures. The authors declare that the work described in this paper is protected by a pending patent.

Data availability. The data that support the plots within this paper are available from the corresponding author upon reasonable request.

References

1. R. Marchetti, C. Lacava, L. Carroll, *et al.*, "Coupling strategies for silicon photonics integrated chips [Invited]," Photonics Res. **7**(2), 201–239 (2019).
2. L. Cheng, S. Mao, Z. Li, *et al.*, "Grating couplers on silicon photonics: design principles, emerging trends and practical issues," Micromachines **11**(7), 666 (2020).
3. C. V. Poulton, A. Yaacobi, D. B. Cole, *et al.*, "Coherent solid-state LIDAR with silicon photonic optical phased arrays," Opt. Lett. **42**(20), 4091–4094 (2017).
4. Z. Zhang, S. Mouradian, F. N. C. Wong, *et al.*, "Entanglement-enhanced sensing in a lossy and noisy environment," Phys. Rev. Lett. **114**(11), 110506 (2015).
5. Y. Ding, H. Ou, C. Peucheret, *et al.*, "Fully-etched apodized fiber-to-chip grating coupler on the SOI platform with −0.78 dB coupling efficiency using photonic crystals and bonded Al mirror," in *2014 The European Conference on Optical Communication (ECOC)* (2014), pp. 1–3.
6. W. S. Zaoui, A. Kunze, W. Vogel, *et al.*, "Bridging the gap between optical fibers and silicon photonic integrated circuits," Opt. Express **22**(2), 1277–1286 (2014).
7. D. Benedikovic, P. Cheben, J. H. Schmid, *et al.*, "Subwavelength index engineered surface grating coupler with sub-decibel efficiency for 220-nm silicon-on-insulator waveguides," Opt. Express **23**(17), 22628–22635 (2015).
8. N. Hoppe, W. S. Zaoui, L. Rathgeber, *et al.*, "Ultra-efficient silicon-on-insulator grating couplers with backside metal mirrors," IEEE J. Sel. Top. Quantum Electron. **26**(2), 1–6 (2020).
9. E. Lomonte, M. Stappers, L. Krämer, *et al.*, "Scalable and efficient grating couplers on low-index photonic platforms enabled by cryogenic deep silicon etching," Sci. Rep. **14**(1), 4256 (2024).
10. Y. Wang, H. Yun, Z. Lu, *et al.*, "Apodized focusing fully etched subwavelength grating couplers," IEEE Photonics J. **7**(6), 1–8 (2015).

Optics EXPRESS

11. D. Taillaert, P. Bienstman, and R. Baets, "Compact efficient broadband grating coupler for silicon-on-insulator waveguides," Opt. Lett. **29**(23), 2749–2751 (2004).
12. S. K. Selvaraja, D. Vermeulen, M. Schaekers, *et al.*, "Highly efficient grating coupler between optical fiber and silicon photonic circuit," in *Conference on Lasers and Electro-Optics/International Quantum Electronics Conference (2009), Paper CTuC6* (Optica Publishing Group, 2009), p. CTuC6.
13. A. Mekis, S. Abdalla, D. Foltz, *et al.*, "A CMOS photonics platform for high-speed optical interconnects," in *IEEE Photonics Conference 2012* (2012), pp. 356–357.
14. X. Chen, C. Li, C. K. Y. Fung, *et al.*, "Apodized waveguide grating couplers for efficient coupling to optical fibers," IEEE Photonics Technol. Lett. **22**(15), 1156–1158 (2010).
15. A. Mekis, S. Gloeckner, G. Masini, *et al.*, "A grating-coupler-enabled CMOS photonics platform," IEEE J. Sel. Top. Quantum Electron. **17**(3), 597–608 (2011).
16. D. Fowler, P. Grosse, F. Gays, *et al.*, "Fiber grating coupler development for Si-photonics process design kits at CEA-LETI," in *Smart Photonic and Optoelectronic Integrated Circuits XXI* (SPIE, 2019), 10922, pp. 19–25.
17. W. D. Sacher, Y. Huang, L. Ding, *et al.*, "Wide bandwidth and high coupling efficiency Si_3N_4-on-SOI dual-level grating coupler," Opt. Express **22**(9), 10938–10947 (2014).
18. G. Roelkens, D. V. Thourhout, and R. Baets, "High efficiency Silicon-on-Insulator grating coupler based on a poly-Silicon overlay," Opt. Express **14**(24), 11622–11630 (2006).
19. C. Alonso-Ramos, P. Cheben, A. Ortega-Moñux, *et al.*, "Fiber-chip grating coupler based on interleaved trenches with directionality exceeding 95%," Opt. Lett. **39**(18), 5351–5354 (2014).
20. D. Benedikovic, C. Alonso-Ramos, P. Cheben, *et al.*, "High-directionality fiber-chip grating coupler with interleaved trenches and subwavelength index-matching structure," Opt. Lett. **40**(18), 4190–4193 (2015).
21. Y. Chen, R. Halir, Í. Molina-Fernández, *et al.*, "High-efficiency apodized-imaging chip-fiber grating coupler for silicon nitride waveguides," Opt. Lett. **41**(21), 5059–5062 (2016).
22. J. Notaros, F. Pavanello, M. T. Wade, *et al.*, "Ultra-Efficient CMOS Fiber-to-Chip Grating Couplers," in *Optical Fiber Communication Conference (2016)*, Paper M2I.5 (Optica Publishing Group, 2016), p. M2I.5.
23. T. Watanabe, M. Ayata, U. Koch, *et al.*, "Perpendicular Grating Coupler Based on a Blazed Antiback-Reflection Structure," J. Lightwave Technol. **35**(21), 4663–4669 (2017).
24. X. Chen, D. J. Thomson, L. Crudginton, *et al.*, "Dual-etch apodised grating couplers for efficient fibre-chip coupling near 1310 nm wavelength," Opt. Express **25**(15), 17864–17871 (2017).
25. M. Raval, C. V. Poulton, and M. R. Watts, "Unidirectional waveguide grating antennas with uniform emission for optical phased arrays," Opt. Lett. **42**(13), 2563–2566 (2017).
26. L. Su, R. Trivedi, N. V. Sapra, *et al.*, "Fully-automated optimization of grating couplers," Opt. Express **26**(4), 4023–4034 (2018).
27. D. Benedikovic, C. Alonso-Ramos, S. Guerber, *et al.*, "Sub-decibel silicon grating couplers based on L-shaped waveguides and engineered subwavelength metamaterials," Opt. Express **27**(18), 26239 (2019).
28. P. Ma, P. Wang, M. Wang, *et al.*, "A SiN antenna based on grating–waveguide–grating structure for unidirectional and uniform emission," Opt. Commun. **527**, 128959 (2023).
29. R. Guo, S. Zhang, H. Gao, *et al.*, "Blazed subwavelength grating coupler," Photonics Res. **11**(2), 189–195 (2023).
30. J. Schrauwen, F. Van Laere, D. Van Thourhout, *et al.*, "Focused-ion-beam fabrication of slanted grating couplers in silicon-on-insulator waveguides," IEEE Photonics Technol. Lett. **19**(11), 816–818 (2007).
31. A. Hadij-ElHouati, P. Cheben, A. Ortega-Moñux, *et al.*, "High-efficiency conversion from waveguide mode to an on-chip beam using a metamaterial engineered Bragg deflector," Opt. Lett. **46**(10), 2409–2412 (2021).
32. T. Tamir and S. T. Peng, "Analysis and design of grating couplers," Appl. Phys. **14**(3), 235–254 (1977).
33. "Ohara," https://www.ohara-inc.co.jp/en/product/opticalglass/.
34. A. Sánchez-Postigo, R. Halir, J. G. Wangüemert-Pérez, *et al.*, "Breaking the coupling efficiency–bandwidth trade-off in surface grating couplers using zero-order radiation," Laser Photonics Rev. **15**(6), 2000542 (2021).
35. R. Halir, P. Cheben, S. Janz, *et al.*, "Waveguide grating coupler with subwavelength microstructures," Opt. Lett. **34**(9), 1408–1410 (2009).
36. R. Halir, P. J. Bock, P. Cheben, *et al.*, "Waveguide sub-wavelength structures: a review of principles and applications," Laser Photonics Rev. **9**(1), 25–49 (2015).
37. J. M. Luque-González, A. Sánchez-Postigo, A. Hadij-ElHouati, *et al.*, "A review of silicon subwavelength gratings: building break-through devices with anisotropic metamaterials," Nanophotonics **10**(11), 2765–2797 (2021).
38. P. Cheben, J. H. Schmid, R. Halir, *et al.*, "Recent advances in metamaterial integrated photonics," Adv. Opt. Photonics **15**(4), 1033–1105 (2023).
39. L. Zavargo-Peche, A. Ortega-Monux, J. G. Wanguemert-Perez, *et al.*, "Fourier based combined techniques to design novel sub-wavelength optical integrated devices," Prog. Electromagn. Res. **123**, 447–465 (2012).
40. "FullWAVE FDTD Simulation Software - RSoft Photonic Device Tools | Synopsys Photonic Solutions," https://www.synopsys.com/photonic-solutions/rsoft-photonic-device-tools/passive-device-fullwave.html.
41. S. R. Bickham, M. A. Marro, J. A. Derick, *et al.*, "Reduced cladding diameter fibers for high-density optical interconnects," J. Lightwave Technol. **38**(2), 297–302 (2020).
42. P. Ginel-Moreno, D. Pereira-Martín, A. Hadij-ElHouati, *et al.*, "Highly efficient optical antenna with small beam divergence in silicon waveguides," Opt. Lett. **45**(20), 5668–5671 (2020).

Optics EXPRESS

43. P. Ginel-Moreno, A. Sánchez-Postigo, J. de-Oliva-Rubio, *et al.*, "Millimeter-long metamaterial surface-emitting antenna in the silicon photonics platform," Opt. Lett. **46**(15), 3733–3736 (2021).
44. S. A. Miller, Y.-C. Chang, C. T. Phare, *et al.*, "Large-scale optical phased array using a low-power multi-pass silicon photonic platform," Optica **7**(1), 3–6 (2020).
45. A. Taflove and S. C. Hagness, *Computational Electrodynamics: The Finite-Difference Time-Domain Method, Artech House Antennas and Propagation Library* (Artech House, 2005).
46. K.-W. Zhao and J.-W. Pan, "Optical design for a see-through head-mounted display with high visibility," Opt. Express **24**(5), 4749–4760 (2016).
47. "High refractive index printing material for microoptics: IP-n162," https://www.nanoscribe.com/en/products/ip-photoresins/ip-n162/#:~:text=IP%2Dn162%20has%20a%20high,an%20Abbe%20number%20of%2025.
48. F. van Schoonhoven, Y. Tomishige, A. Abazi, *et al.*, "Inkjet-printed waveguide-coupled passive wedge-shaped microdisk resonator with refractive index tunability," Opt. Mater. Express **14**(7), 1767–1778 (2024).
49. J. M. Laniel, J.-M. Ménard, K. Turcotte, *et al.*, "Refractive index measurements of planar chalcogenide thin film," J. Non-Cryst. Solids **328**(1-3), 183–191 (2003).